

Simulation, design, and first test of a multi-energy soft x-ray (SXR) pinhole camera in the Madison Symmetric Torus (MST)

L. F. Delgado-Aparicio, J. Wallace, H. Yamazaki, P. VanMeter, L. Reusch, M. Nornberg, A. Almagari, J. Maddox, B. Luethi, M. Rissi, T. Donath, D. Den Hartog, J. Sarff, P. Weix, J. Goetz, N. Pablant, K. Hill, B. Stratton, P. Efthimion, Y. Takase, A. Ejiri, and M. Ono

Citation: [Review of Scientific Instruments](#) **89**, 10G116 (2018); doi: 10.1063/1.5038798

View online: <https://doi.org/10.1063/1.5038798>

View Table of Contents: <http://aip.scitation.org/toc/rsi/89/10>

Published by the [American Institute of Physics](#)

Articles you may be interested in

[A computational tool for simulation and design of tangential multi-energy soft x-ray pin-hole cameras for tokamak plasmas](#)

[Review of Scientific Instruments](#) **89**, 10G120 (2018); 10.1063/1.5038788

[Pixel-to-pixel variation on a calibrated PILATUS3-based multi-energy soft x-ray detector](#)

[Review of Scientific Instruments](#) **89**, 10G119 (2018); 10.1063/1.5037347

[Application of the VUV and the soft x-ray systems on JET for the study of intrinsic impurity behavior in neon seeded hybrid discharges](#)

[Review of Scientific Instruments](#) **89**, 10D131 (2018); 10.1063/1.5038930

[Utilization of outer-midplane collector probes with isotopically enriched tungsten tracer particles for impurity transport studies in the scrape-off layer of DIII-D \(invited\)](#)

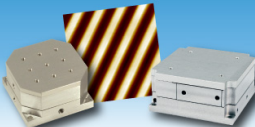
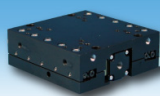
[Review of Scientific Instruments](#) **89**, 10I115 (2018); 10.1063/1.5039347

[Motional Stark effect imaging first results on the DIII-D tokamak](#)

[Review of Scientific Instruments](#) **89**, 10D124 (2018); 10.1063/1.5038969

[Design of tangential x-ray crystal spectrometer for Aditya-U tokamak](#)

[Review of Scientific Instruments](#) **89**, 10F115 (2018); 10.1063/1.5039359



Nanopositioning Systems Micropositioning AFM & SPM Single molecule imaging

Simulation, design, and first test of a multi-energy soft x-ray (SXR) pinhole camera in the Madison Symmetric Torus (MST)

L. F. Delgado-Aparicio,^{1,a)} J. Wallace,² H. Yamazaki,³ P. VanMeter,² L. Reusch,² M. Nornberg,² A. Almagari,² J. Maddox,² B. Luethi,⁴ M. Rissi,⁴ T. Donath,⁴ D. Den Hartog,² J. Sarff,² P. Weix,² J. Goetz,² N. Pablant,¹ K. Hill,¹ B. Stratton,¹ P. Efthimion,¹ Y. Takase,³ A. Ejiri,³ and M. Ono¹

¹Princeton Plasma Physics Laboratory, Princeton, New Jersey 08540, USA

²University of Wisconsin-Madison, Madison, Wisconsin 53706, USA

³The University of Tokyo, Kashiwa 277-8561, Japan

⁴DECTRIS Ltd., 5405 Baden-Dattwil, Switzerland

(Presented 19 April 2018; received 5 May 2018; accepted 20 June 2018; published online 8 October 2018)

A multi-energy soft x-ray pinhole camera has been designed and built for the Madison Symmetric Torus reversed field pinch to aid the study of particle and thermal-transport, as well as MHD stability physics. This novel imaging diagnostic technique combines the best features from both pulse-height-analysis and multi-foil methods employing a PILATUS3 x-ray detector in which the lower energy threshold for photon detection can be adjusted independently on each pixel. Further improvements implemented on the new cooled systems allow a maximum count rate of 10 MHz per pixel and sensitivity to the strong Al and Ar emission between 1.5 and 4 keV. The local x-ray emissivity will be measured in multiple energy ranges simultaneously, from which it is possible to infer 1D and 2D simultaneous profile measurements of core electron temperature and impurity density profiles with no *a priori* assumptions of plasma profiles, magnetic field reconstruction constraints, high-density limitations, or need of shot-to-shot reproducibility. The expected time and space resolutions will be 2 ms and <1 cm, respectively. *Published by AIP Publishing.* <https://doi.org/10.1063/1.5038798>

I. MOTIVATION

A collaboration between PPPL, the Physics Department at the University of Wisconsin-Madison, and the University of Tokyo has been established to design, build, install, and operate a multi-energy (ME) soft x-ray (SXR) pinhole camera at the Madison Symmetric Torus (MST) Reversed Field Pinch (RFP).¹ This novel ME-SXR diagnostic has the capability to measure the x-ray emissivity in multiple energy ranges simultaneously, from which is possible to infer profile measurements of core electron temperature (T_e) and impurity density (n_Z) with no *a priori* assumptions of plasma profiles, magnetic field reconstruction constraints, high-density limitations, or need of shot-to-shot reproducibility.

Further improvements implemented on the new cooled PILATUS3 systems² allows to be sensitive to the strong aluminum emission between 1.5 and 2.4 keV. The latter arises from the interaction between the plasma and Al ions sputtered from the exposure of the plasma to the vacuum vessel. The strong emission [see Figs. 1(a) and 1(b)] from the Al recombination edges as well as line-radiation from He-like and H-like charge states—commonly found at temperatures from 0.5 to 1-2 keV [see Fig. 2(a)]—has been a persistent challenge in the interpretation of MST's x-ray data for many years. The benefit to the MST program lies, therefore, in the ability of

the new detector to characterize the Al line-radiation present in MST which nicely complements the data obtained with the existent two-color diode array suite which uses conventional Be filters with 50% transmission at 4 and 5 keV.³⁻⁹

The strong line-emission of Ar and Mo shown in Figs. 1(c) and 1(d)—characteristic of He- and H-like Ar as well as Ne-like Mo charge states [see Figs. 2(b) and 2(c)]—will also be spatially resolved and time-resolved, thus facilitating impurity transport experiments. To account for the natural increase in signals in comparison with the weak hydrogenic bremsstrahlung, we will make use of the newly developed instant re-trigger technology, which detects pulse pile-up, retriggers the counting circuit, and effectively overcomes counter paralysis. Photon rates up to 10^7 photons/s in a single pixel can be accurately measured.

II. METHODOLOGY

The proposed system will monitor the radial time history profiles of the medium-Z emission at multiple energy ranges in all MST scenarios. The detector allows the user to set pixels at different energy ranges according to characteristic cutoff-energies (E_c) or thresholds, with the response widths of ~ 0.5 keV. The ability to set an energy threshold at an arbitrary value with constant energy resolution is a significant improvement over metallic foil systems.⁵⁻⁹ In principle, a larger number of pixels can be set to the higher energy threshold to compensate for the exponential decrease in the photon intensity with energy.

Note: Paper published as part of the Proceedings of the 22nd Topical Conference on High-Temperature Plasma Diagnostics, San Diego, California, April 2018.

^{a)}Electronic mail: ldelgado@pppl.gov

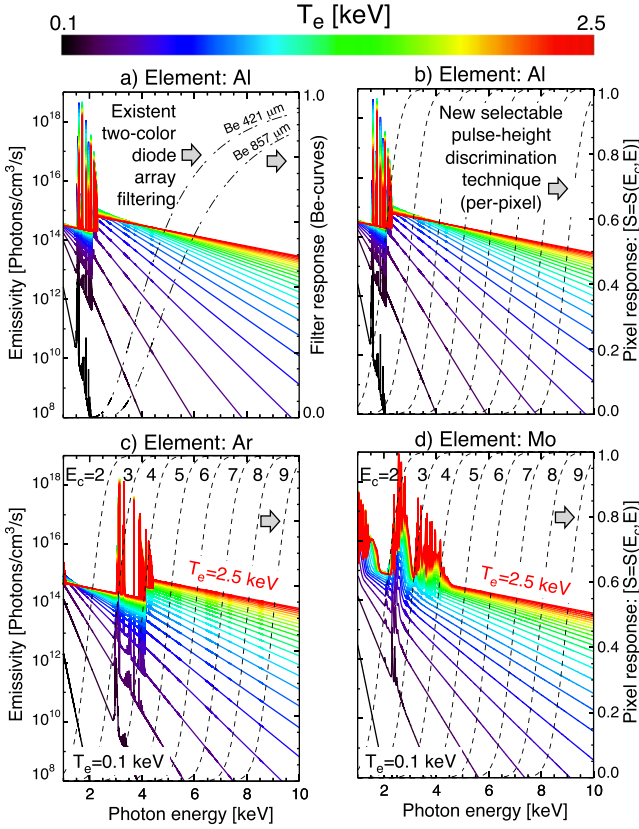


FIG. 1. FLYCHK x-ray spectra for (a) and (b) Al, (c) Ar, and (d) Mo at multiple values of electron temperatures between 0.1 and 2.5 keV. The dotted lines in (b)–(d) are the pixel response curves between 2 and 9 keV.

A. Spectroscopy

The x-ray spectra emitted by hot plasmas are characterized by a set of continua that falls off exponentially with increasing photon energy and decreasing electron temperature. Bremsstrahlung (free-free) and radiative recombination (free-bound) are the two dominant emission processes contributing to the continuum radiation and can be expressed as

$$\frac{d\mathcal{P}_{FF}^{ij}}{dE} \propto \frac{n_e^2}{T_e^{1/2}} \frac{n_i}{n_e} \frac{n_{ij}}{n_i} Z_{ij}^2 \mathcal{G}_{ff}(Z, T_e, E) \exp(-E/T_e), \quad (1)$$

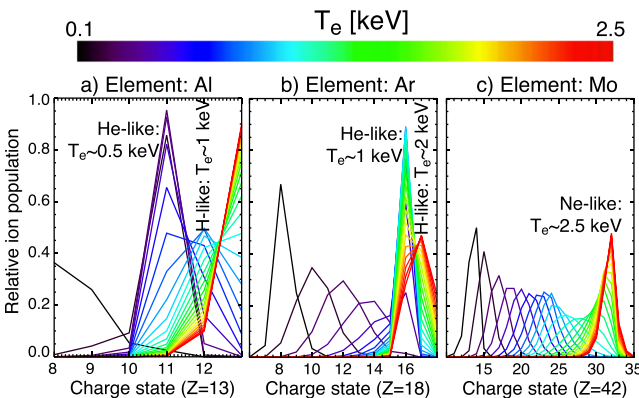


FIG. 2. FLYCHK relative ion population for Al, Ar, and Mo at values of T_e between 0.1 and 2.5 keV. Charge-state balance does not include the effects from the neutral charge exchange and background transport.

$$\frac{d\mathcal{P}_{FB}^{ij}}{dE} \propto \frac{n_e^2}{T_e^{1/2}} \frac{n_i}{n_e} \frac{n_{ij}}{n_i} Z_{ij}^2 \beta_{ij}(T_e, E) \exp(-E/T_e), \quad (2)$$

where n_i/n_e is the impurity concentration, n_{ij}/n_i is the ion charge state distribution, \mathcal{G}_{FF} is the free-free Gaunt-factor, and β_{ij} represents recombination from all quantum states. Line-emission (bound-bound radiation) is the third mechanism occurring in hot plasmas and is always visible above the continuum. The power radiated per unit energy by an impurity ion i in a charge state j can be expressed as

$$\frac{\mathcal{P}_L^{ij}}{E_L} \propto n_e^2 \frac{n_i}{n_e} \frac{n_{ij}}{n_i} \langle \sigma v(T_e, E)_{ij} \rangle, \quad (3)$$

where $\langle \sigma v(T_e, E)_{ij} \rangle$ is the total cross section averaged over a Maxwellian velocity distribution.

The spectra depicted in Fig. 1 show the continuum- and line-emissivities of Al, Ar, and Mo as a function of photon energy between 1 and 10 keV, for electron temperatures between 0.1 and 2.5 keV, an electron density of $1.0 \times 10^{14} \text{ cm}^{-3}$, and impurity concentrations of 10^{-6} , as calculated by the FLYCHK code.¹⁰ Choosing a detector response with cutoff energies below 4 keV can be used to calculate Al impurity concentrations. However, preselecting a detector response counting photons with energies stronger than 4 keV will help to eliminate the “contamination” by the Al line-emission, thus facilitating the temperature profile measurements.

B. Geometrical considerations: Tangential vs radial views

The MST geometry and magnetic field configuration are shown in Fig. 3(a). Conventional wisdom suggests that the choice of a tangential view has several advantages over that of a radial view since the goal is to accurately resolve the $\Delta R \sim 90 \text{ cm}$ spanning from the inboard to the outboard side using the 487 columns of the PILATUS3 detector. However, most of the high-confinement regimes in MST show a strong $n = 6$ toroidal component for standard reversed plasmas and PPCD scenarios and $n = 5$ for non-reversed plasmas only (of which quasi-single helicity plasmas are a high-current subset). This distortion from equilibrium therefore invalidates

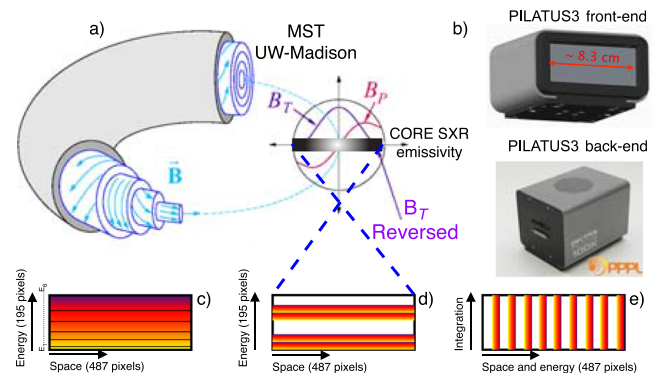


FIG. 3. (a) Cross section of MST highlighting the mid-plane core region. (b) Separable PILATUS3 front- and back-end electronics. Three distinct pixel maps will have [(c) and (d)] high- and (e) medium-spatial resolution, respectively.

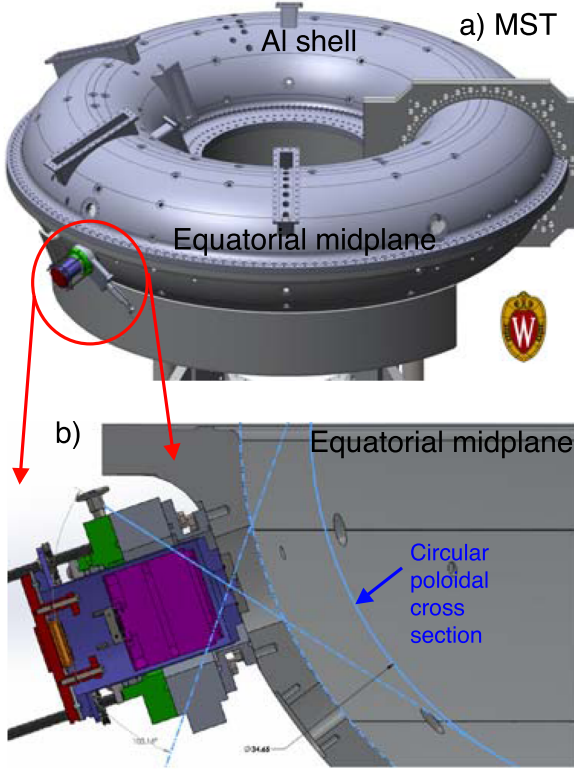


FIG. 4. Radial view located under the equatorial mid-plane imaging the entire circular cross section of MST plasmas. The detector is placed vertically, and the pixel settings will be arranged as shown in Figs. 3(d) and 3(e).

the toroidal axisymmetric assumption and limits the use of a tangential configuration and its Abel-formalism.

A ME-SXR system with a radial view was tested successfully at Alcator C-Mod⁸ using a $\sim 24 \text{ cm}^2$ PILATUS detector in combination with a 1 mm tall horizontal slit placed after a Be vacuum-wall filter. A nearly identical configuration will be used at MST. The orientation of the slit parallel to the toroidal magnetic field is possible because n_e and T_e and therefore the x-ray emission are uniform along the toroidal field. The measured profiles are thus spatially resolved in a direction perpendicular to the toroidal magnetic field. The x-ray camera is designed to take an image of the nearly circular poloidal cross section (see Fig. 4) in scenarios with or without the $m = 1$ poloidal component.

III. SIMULATIONS OF MST CIRCULAR PLASMAS

A. Input profiles for simulations

The input profiles used for evaluating the detector response are shown in Fig. 5. The family of curves describing the density and temperature profiles are shown in Fig. 5(c), with basic parameters $\alpha = 8$ and $\beta = 2$ and edge offsets of the order of $0.5 \times 10^{16} \text{ m}^{-3}$ and 0.1 keV, respectively. The three cases considered are

- CASE 1: DCO plasma. Using deuterium and carbon (D) and oxygen (O) concentrations of 2.5% and 0.05% which result in a core $Z_{eff,0} \sim 2.03$.

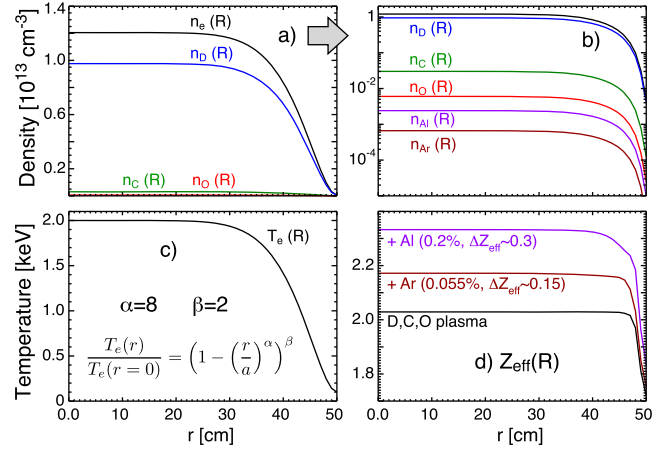


FIG. 5. Density, T_e , and Z_{eff} profiles used for the three simulation cases: DCO, DCO + Al, and DCO + Ar.

- CASE 2: DCO plasma + Al. Adding a small constant concentration of aluminum of the order of 0.2% which increases the core Z_{eff} to ~ 2.33 .
- CASE 3: DCO plasma + Ar. Adding a small constant concentration of argon of the order of 0.055% which increases the core Z_{eff} from ~ 2.03 to ~ 2.17 .

B. Calculating local emissivities for arbitrary plasmas

A large database has been created using the FLYCHK code for calculating the SXR emission from several ions (e.g., D, C, O, Al, Si, Ar, Ca, Fe, Ni, Mo, and W). The goal of this numerical exercise is to simulate the detector response under various plasma profiles and arbitrary impurity concentrations. The number of x-ray photons emitted by a volume-element which are subsequently detected by a photon counting system is given by⁸

$$\mathcal{E}_i = \int_{E_0}^{E_1} \frac{\mathcal{F}_i(n_{e,i}, T_e, E)}{E} \mathcal{T}_{Be} \mathcal{T}_V \mathcal{A}_{Si} \mathcal{S}_{Det}(E_c, E) dE, \quad (4)$$

where \mathcal{F}_i is the FLYCHK emissivity for the i th species, $\mathcal{T}_{Be}(E) \cdot \mathcal{T}_V(E)$ is the transmission product of the Be-filter and vacuum, $\mathcal{A}_{Si}(E)$ is the x-ray absorption in the silicon detector lattice, and $\mathcal{S}_{det}(E_c, E)$ are the detector electronic response curves shown with dotted lines in Figs. 1(b)–1(d). The spectral calibration of this system was performed at the DECTRIS laboratories and is presented as a separated contribution in these proceedings.¹¹

The total emission is the sum of the emission over all the ion species,

$$\mathcal{E}(R, Z) = \sum_i^n \mathcal{E}_i(R, Z). \quad (5)$$

For simplicity, we assume a constant concentration of background low- Z impurities like C and O as well as additional intrinsic and extrinsic impurities such as Al and Ar (e.g., gas-puff for diagnostics). As such, the resultant local deuterium concentration and plasma charge can be calculated using quasineutrality,

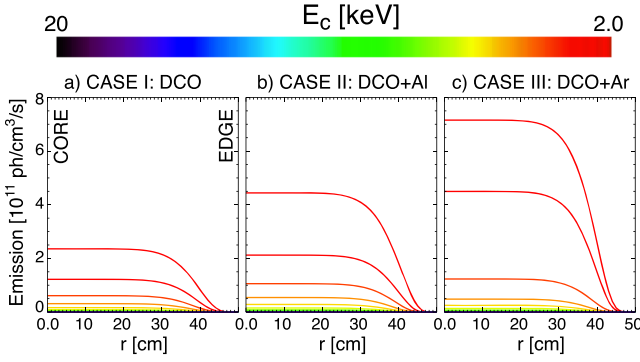


FIG. 6. SXR emission for the three simulation cases: DCO, DCO + Al, and DCO + Ar.

$$\frac{n_D}{n_e} = 1 - \sum_i^n \frac{n_{Z_i}}{n_e} \cdot \langle Z \rangle_{\mathcal{F}_i}(T_e), \quad (6)$$

$$Z_{\text{eff}} = \frac{n_D}{n_e} + \sum_i^n \frac{n_{Z_i}}{n_e} \cdot \langle Z \rangle_{\mathcal{F}_i}^2(T_e), \quad (7)$$

where $\langle Z \rangle_{\mathcal{F}_i}$ is the FLYCHK average charge of the i th ion as a function of the local electron temperature.

The SXR emission profiles computed for the three cases listed above—as a function of different pixel cutoff energies from 2 to 20 keV—are shown in Fig. 6. A small quantity of Al and Ar ions—nearly double or triple that of the “clean” DCO background plasma. A stronger contrast will be obtained if the background Z_{eff} approaches unity. The sensitivity to aluminum can also be increased by using lower energy thresholds (e.g., $E_c = 1.6$ keV instead of $E_c = 2$ keV) since its strongest line-radiation stems from photon energies between 1.5 and 2 keV. In addition, we expect to find a strong contribution from the Al recombination between ~ 2.1 keV and ~ 2.3 keV. This enhancement corresponds to the radiative capture of free electrons by hydrogen-like Al into the ground state of helium-like Al.¹²

C. 1D imaging of MST’s circular poloidal cross section

The matrix-based inversion technique used hereafter has been described by Bell¹³ and has already been applied to tangential imaging of charge exchange recombination spectroscopy, soft and hard x-rays, and bolometric measurements. In such formalism, the brightness and inverted emission can be easily expressed as

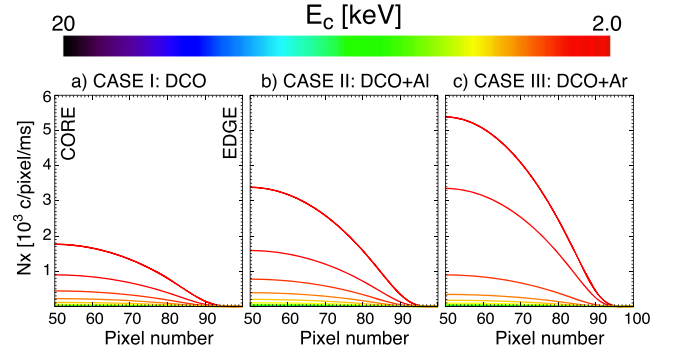


FIG. 7. Number of x-ray photons (or counts) for the three simulation cases: DCO, DCO + Al, and DCO + Ar.

$$\mathcal{B}_i = \sum_j \mathcal{L}_{ij} \mathcal{E}_j \Rightarrow \mathcal{E}_j = \sum_i \mathcal{L}_{ji}^{-1} \mathcal{B}_i, \quad (8)$$

where \mathcal{L} is the length matrix. In addition, the number of x-ray photons \mathcal{N}^X measured by each pixel is given by the product of the brightness, the *étendue*, and the integration time Δt ,

$$\mathcal{N}_i^X = \mathcal{B}_i \cdot \eta(\theta_i) \cdot \Delta t, \quad (9)$$

$$\eta(\theta_i) \approx \frac{A_{\text{pin}} \cdot A_{\text{pix}}}{4\pi d^2} \cos^4 \theta_i, \quad (10)$$

where A_{pin} is the area of the pin-hole, A_{pix} is the area of the pixel, and d is the characteristic distance between the center of the detector and the pin-hole; θ_i for each integration sightline is the angle subtended between the normal of the pinhole and each of the other pixels of the detector array. The number of x-ray photons computed for the three cases described above as a function of different pixel cutoff energies from 2 to 20 keV is shown in Fig. 7. The values of the pin-hole and pixel areas used in this simulation are $1 \text{ mm} \times 4 \text{ mm} = 4 \text{ mm}^2$ and $0.172 \text{ mm} \times 0.172 \text{ mm} \approx 2.96 \times 10^{-2} \text{ mm}^2$, respectively. Also, the distance between the pin-hole and detector is approximately 30.5 mm, so the central *étendue* is approximately $1.012 \times 10^{-7} \text{ cm}^2$. The simulation carried out only considered 101 sight-lines separated by nearly 1 cm from $r \in [-50, 50]$ cm. Since the detector has nearly 500 pixels in the vertical direction, one can expect using up to five energy ranges and still make images of the plasma emission with a spatial resolution of about ~ 1 cm.

IV. COMPACT CAMERA AND FIRST TEST

The design of a very compact multi-energy SXR pin-hole camera for MST is shown in Figs. 8 and 9. The PILATUS3

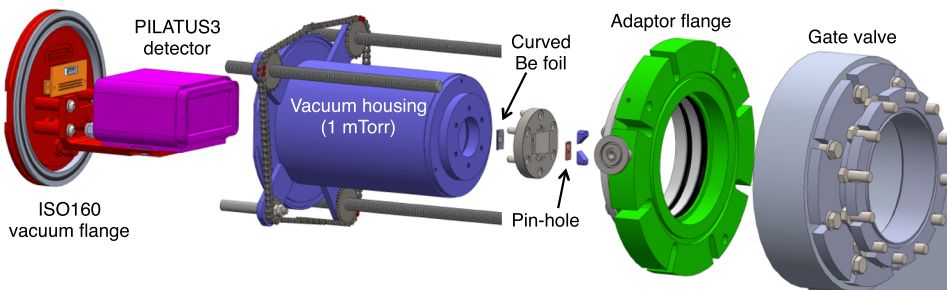


FIG. 8. Exploded view of ME-SXR at MST showing the ISO160 vacuum flange with differential pumping and cooling lines, as well as power and data transfer connectors, the PILATUS3 detector, the vacuum housing enclosure, the curved Be 25 μ foil, the $1 \times 4 \text{ mm}^2$ pinhole, the adaptor flange, and the gate valve.

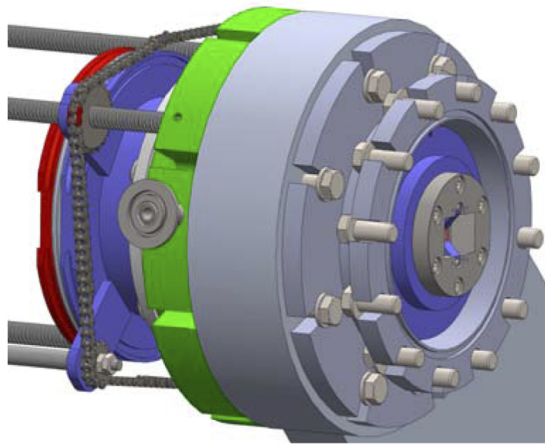
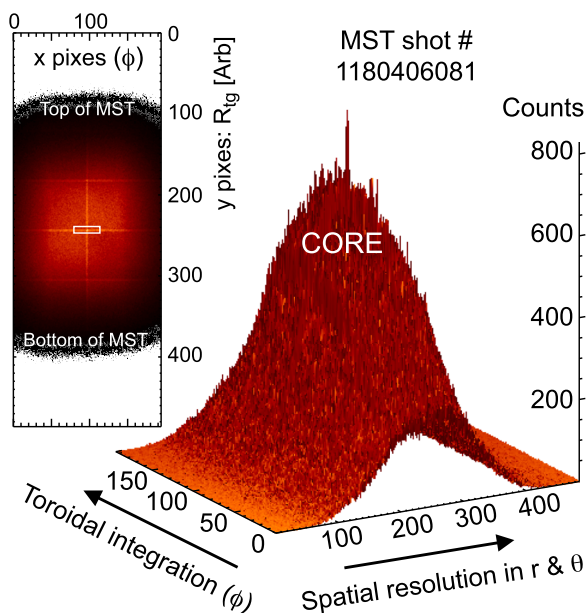


FIG. 9. Compact ME-SXR detector for MST.

FIG. 10. First brightness profile data obtained with constant $E_c = 4$ keV across the 2D detector.

detector sits in an Al-shelf attached to the stainless steel ISO160 vacuum flange. This flange has been machined with a port for differential pumping and two water-cooling lines, as well as power and data transfer connectors. The aluminum detector housing will be kept at a diagnostic vacuum of 1 mTorr separating the machine vacuum by a curved $25 \mu\text{m}$ thick Be filter which acts as the main vacuum-wall interface. The vacuum housing is designed to slide through the adaptor flange when the gate valve opens. Two o-rings ensure vacuum while differential pumping is applied through a side-valve on the

adaptor flange. When collapsed, the compact system is shorter than 15 cm.

The first data collected with the system installed in the spring of 2018 are shown in Fig. 10. They are from shot 1180406081, with an integration time of 10 ms using a constant detector threshold set to 4 keV and during the early phase of the PPCD discharge at 500 kA. As stated above, integrating photons with energies stronger than 4 keV will help sampling only the continuum avoiding “contamination” by the Al line-emission and thus facilitating the temperature profile measurements. The *spikes* in the data correspond to the data associated with the “pixels” in-between chips, so they are easily removed. Future tests in the spring will optimize the pin-hole and detector geometry as well as use cut-off energies below 2 keV.

V. CONCLUSION

A compact ME-SXR pinhole camera has been designed and built for the MST-RFP to aid the study of particle and thermal-transport, as well as MHD stability physics. This new diagnostic employs a pixelated detector in which the lower threshold for photon detection can be adjusted independently on each pixel allowing a maximum count rate of 10 MHz per pixel and sensitivity to the strong Al emission between 1.5 and 2.4 keV. The local x-ray emissivity will be measured in multiple energy ranges simultaneously, from which it is possible to infer 1D simultaneous profile measurements of T_e , n_{Al} , and Z_{eff} . The expected time and space resolutions will be 2 ms and <1 cm, respectively.

ACKNOWLEDGMENTS

This work is supported by the U.S. DOE-OFES under Contract No. DE-AC02-09CH11466 and LFDA’s 2015 DOE Early Career Award Research Program.

¹J. Sarff *et al.*, *Phys. Rev. Lett.* **72**, 3670 (1994).

²See <https://www.dectris.com> for detailed information of PILATUS3 x-ray detectors.

³L. M. Reusch *et al.*, *Rev. Sci. Instrum.* **85**, 11D844 (2014).

⁴M. Galante *et al.*, *Nucl. Fusion* **55**, 123016 (2015).

⁵L. Delgado-Aparicio *et al.*, *Plasma Phys. Controlled Fusion* **49**, 1245 (2007).

⁶L. Delgado-Aparicio *et al.*, *Rev. Sci. Instrum.* **81**, 10E303 (2010).

⁷L. Delgado-Aparicio *et al.*, PPPL-Report 4977, 2014.

⁸L. Delgado-Aparicio *et al.*, *Rev. Sci. Instrum.* **87**, 11E204 (2016).

⁹H. Yamazaki *et al.*, “A computational tool for simulation and design of tangential multi-energy soft x-ray pin-hole cameras for tokamak plasmas,” *Rev. Sci. Instrum.* (these proceedings).

¹⁰H.-K. Chung *et al.*, *High Energy Density Phys.* **1**, 3 (2005).

¹¹P. vanMeter *et al.*, “Pixel-to-pixel variation on a calibrated PILATUS3-based multi-energy soft x-ray detector,” *Rev. Sci. Instrum.* (these proceedings).

¹²K. Brau *et al.*, *Phys. Rev. A* **22**, 2769 (1980).

¹³R. E. Bell, *Rev. Sci. Instrum.* **66**, 558 (1995).